NEW METHOD FOR SILICON SENSOR CHARGE CALIBRATION USING COMPTON SCATTERING

A PREPRINT

Patrick McCormack[*]
Physics Department
UC Berkeley

Maurice Garcia-Sciveres
Physics Division
Lawrence Berkeley National Lab

Timon Heim
Physics Division
Lawrence Berkeley National Lab

Benjamin Nachman
Physics Division
Lawrence Berkeley National Lab

Magne Lauritzen
Department of Physics and Technology
University of Bergen

June 2, 2020

ABSTRACT

As silicon sensors become increasingly thin, the threshold for charge detection decreases, making a calibration of the sensor's charge sensitivity with traditional sources difficult. We present a new method for charge sensitivity calibration using the Compton scattering of photons emitted from an radioactive source or x-ray generator. The electron scattered from the photon deposits its energy near the point of scattering by ionizing the silicon. An accurate measurement of the scattering angle of the photon, made possible by the use of a spectrometer attached to a pivot, allows for precise knowledge of the deposited charge. In the past, this method has been used for calibration of scintillators, but to our knowledge never for silicon detectors; in particular, here it has been studied using a 150 micron thick silicon sensor on an RD53A readout integrated circuit.

***K*eywords** First keyword · Second keyword · More

1 Introduction

Silicon pixel detectors are an important technology for experiments at the Large Hadron Collider (LHC) at CERN [1], such as ATLAS [2] and CMS [3]. Typically, the detector elements of these experiments closest to the collision region are cylindrical with radii typically of a few centimeters formed by flat sensor elements; they are used for charged particle tracking and vertexing. Hybrid pixel and monolithic active pixel silicon (MAPS) detectors are currently the dominant means by which these experiments can acquire position measurements at such small radii in environments with collision rates and radiation doses provided by the LHC [4, 5, 6, 7, 8]. A hybrid pixel detector was used in the development of this calibration technique, and the geometry of such a detector is show in Fig 1 [9].

The goal of most charged particle trackers is to provide a nondestructive measurement of the particle as it traverses the detector, so a detector with minimal radiation length (X_0) is favored. Thinner sensors also require less voltage to achieve full depletion, leading to greater radiation hardness [13]. Because of this, over the past decades of technological improvement, the silicon sensors used for particle experiment applications have become increasingly thin. While the ionization energy loss ($\mathrm{d}E/\mathrm{d}x$) of particles will not depend on sensor thickness, the total energy deposited in the sensor does.

A typical minimum ionizing particle (MIP) deposits about 0.29 keV of energy per micron traversed, corresponding to about 80 electron-hole (e-h) pairs produced per micron. Throughout this paper, a conversion of 3.6 eV per e-h pair will be assumed. At perpendicular incidence, a MIP will leave about 73 keV of energy, or about 20,000 electron-hole pairs, in a 250 μm sensor. If a 150 μm sensor is used, this drops to about 43 keV of energy or about 12,000 e-h pairs.

[*]wpmccormack@lbl.gov

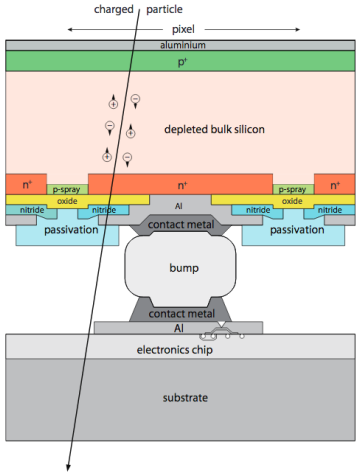

Figure 1: Example geometry of a hybrid pixel detector. A passive silicon sensor is bump-bonded to a readout chip, which serves as the active electronics [9].

The distributions of deposited energy follow Landau distribution functions, so many hits will create fewer e-h pairs than the averages. Additionally, a charged particle may pass through the passive bulk of the sensor corresponding to multiple pixels depending on the particle's incidence angle. If this happens, a hit in a single pixel may only correspond to a fraction of the particle's path length in the sensor. The use of this information can improve position measurement resolution [9]. To achieve maximum detection efficiency for these lower energy pixel hits, the lowest possible operating threshold is favored. Therefore, as sensors become thinner, it becomes necessary to calibrate them to smaller energy deposits.

Current pixel detectors in ATLAS and CMS typically operate with a hit threshold between 2000 e-h pairs and 5000 e-h pairs, depending on the detector layer and year [10, 11, 12]. These thresholds are set to achieve low noise occupancy, as noise can cause fluctuations up to the order of hundreds of e-h pairs. Thresholds are lowered as a function of time due to radiation damage. The thicknesses of sensors used in these experiment's current detectors range from 200 μm to 285 μm, depending on the experiment and location in the detector [4, 5, 6]. For sensors with thickness in the range of 50-150 μm, thresholds may need to be as low or lower than 1000 e-h pairs (3.6 keV) to achieve acceptable efficiency.

The active readout electronics associated with the sensor are typically assumed to be a charge sensitive amplifier with constant reset [22, 23, 24]. The height of the analogue pulse the readout chip receives is proportional to the total charge deposited in the sensor. The pulse is digitized as a time over threshold (ToT) reading. The ToT response for a given charge is manipulated by adjusting both the threshold and the rate of signal dissipation (or return to baseline). The settings for these parameters are usually based on input from an internal charge injection circuit. Charge injection from an external source is a necessary cross-check on this internal circuit.

While sensor calibration has typically relied on techniques such as x-ray absorption [18, 19, 20], absorption of radiation from sources with known energy peaks [16], or calibrations to the energy loss of minimum ionizing particles (MIPs) [17], it is difficult to find a standard method for silicon sensor energy calibration in the range of $\mathcal{O}(1)$ keV or equivalently $\mathcal{O}(1000)$ e-h pairs.

1.1 Compton scattering for calibration

One means of injecting $\mathcal{O}(1)$ keV of energy into a silicon sensor is via the Compton scattering of photons off of the electrons within the sensor. The energy of a photon after Compton scattering off an electron is [14]:

$$E_{\gamma'} = \frac{E_\gamma}{1 + (E_\gamma / m_e c^2)(1 - \cos\theta)}, \tag{1}$$

where $E_{\gamma'}$ is the scattered photon's energy, E_γ is the original energy, and θ is the scattering angle of the photon. The scattered electron acquires the energy $E_\gamma - E_{\gamma'}$. The energy imparted to the electron will be promptly reabsorbed as a localized energy deposit within the sensor. In general, if photons from a source with a peak at $\mathcal{O}(100)$ keV are scattered at angles in the range 5° to 90°, then between approximately 1% and 10% of the initial photon energy can be injected. For example, if a photon from an Americium-241 source, which has an energy peak at 59.5 keV, is scattered at 60°, the electron will have received 3.3 keV of energy. A plot of the energy deposited in the sensor as a function of the

scattering angle for photons from an Americium-241 source is shown in Figure 2. The differential cross-section for Compton scattering is given by the Klein-Nishina formula [15]; the total cross-section for the Compton scattering of an $\mathcal{O}(100)$ keV photon is $\mathcal{O}(1)$ b, varying depending on the energy.

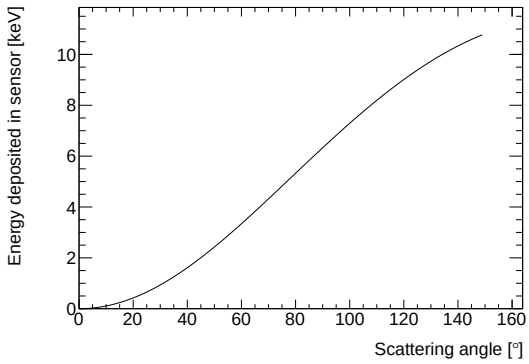

Figure 2: Energy imparted to a silicon sensor as a function of the Compton-scattering angle of 59.5 keV photons emitted from an Americium-241 source.

To precisely know the injected energy, a photodetector can be set to detect photon scatterings into a small angular region. The photodetector can then be used to trigger data readout from the silicon sensor, such that coincident hits in the sensor and photodetector can be correlated. Additionally, the position of the photodetector can be adjusted so that the calibration can be performed over a range of energies.

The precise geometry, instrumentation, and setup used in the development of this method are described in the following sections, as are details relating to the calibration analysis process.

2 Instruments and setup

The sensor used to study this calibration method was a 150 μm silicon sensor manufactured by MPG-HLL [21], which had 100x25 μm pixels. The sensor was bump-bonded onto an RD53A readout integrated circuit (RD53A) with 50x50 μm pixels [22], which served as a readout chip. The total size of the chip is 20.0 mm by 11.6 mm. Readout and tuning were performed by using the YARR software framework [25].

The RD53A is an upgrade development chip designed by a joint collaboration of ATLAS and CMS physicists. It has three front-end types: synchronous, linear, and differential. These are used by the experiments to compare front-end performance in order to select a single type to install in upcoming detector upgrades. In this study, only the differential front end is used. This front end is a pure analogue circuit that implements a readout threshold by unbalancing two branches of an input signal with a differential gain stage [22]. The energy of sensor hits is measured with time over threshold (ToT), which is given in cycles of the 40 MHz chip clock. ToT is stored as a 4-bit output in the datastream. Examples of the ToT response to injected charge for a particular tuning will be shown in Section 3.

Every pixel in the RD53A has a charge-injection circuit, which is used for a pixel-by-pixel tuning. The schematic of this circuit is shown in Figure 3. Two input DC voltages produce a precise differential voltage used for charge injections. By adjusting both the signal threshold and the pulse diffusion rate, the 4-bit ToT output can be adjusted to cover a variety of energy ranges. The RD53A is capable of tuning to thresholds of $\mathcal{O}(100)$ electrons. For the differential front-end, the functional relationship between input charge and ToT (and its inverse) is non-linear and pixel dependent. This means that for precise calibration purposes, every pixel has a unique ToT-to-energy conversion function.

In typical running, RD53A can self-trigger readout based on sensor hits. However, it can also be externally triggered by an LVDS input pulse. The YARR interfacing software includes settings and scans based on such external triggering.

To detect scattered photons, an Amptek X-123 x-ray spectrometer with a 5 mm x 5mm CdTe detector element was used [26]. This spectrometer has auxiliary ports that allow for the output of a simple logic pulse whenever a photon is detected within a certain energy range, which was the external trigger for the RD53A.

A picture and diagram of the experimental setup from above is presented in Figure 4. The equipment is laid out on a 1" x 1" grid of holes to enable easier measurements of distances. An Americium-241 source with activity of 3.2 Ci/g is placed on one end of the grid; there is a small aperture in a piece of brass shielding in front of the source that creates a narrow beam of photons. The peak energy of photons from Americium-241 is 59.5 keV, with a measured

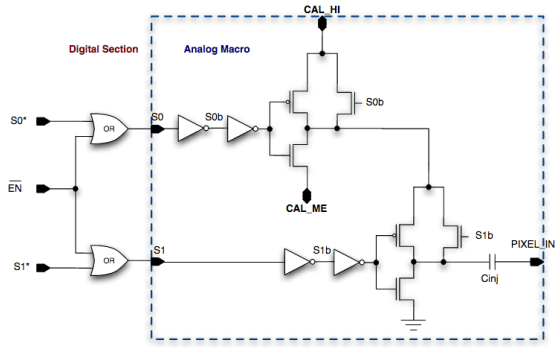

Figure 3: Schematic of the calibration injection circuit in each pixel of the RD53A readout integrated circuit.

FWHM of 0.55 keV. The photons pass through an additional brass collimator with a diameter of 1/4" before falling on the silicon sensor. The sensor is bump-bonded to an RD53A, which is on a custom single chip hybrid PCB board. The spectrometer is mounted on a single arm pivot with rotation point below the sensor, which allows the angle of the scattered-photon acceptance window to be easily adjusted. During data taking, the setup is covered by a box to block out light which could be a background to the silicon sensor and spectrometer. The scattering of photons from the collimator, RD53A, and support structures are an additional background for the spectrometer.

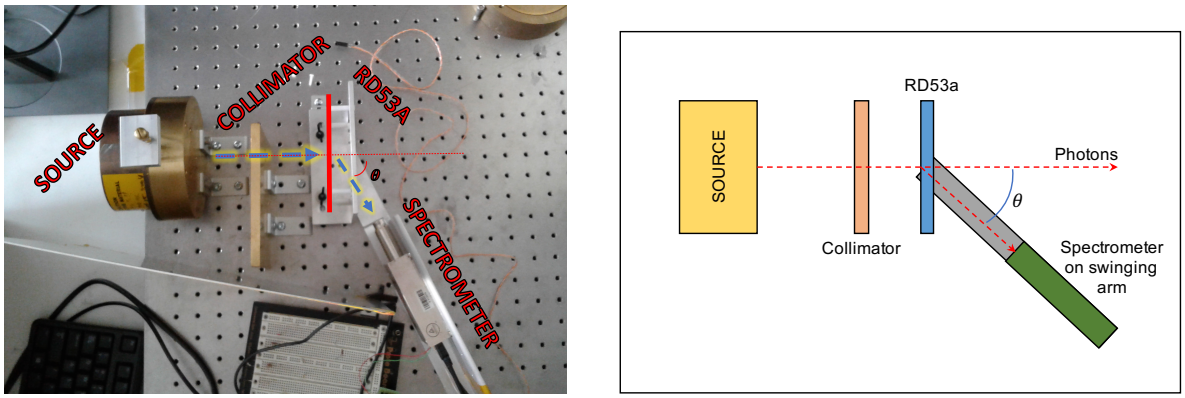

(a) (b)

Figure 4: (a) Aerial picture of the experimental setup with labels. 59.5 keV photons are emitted from an Americium source, pass through a brass collimator, scatter off of the silicon sensor bump bonded to the RD53A, and are detected by the spectrometer. (b) Diagram of setup.

2.1 Spectrometer readout

An example of the spectrometer's readout, as seen in the native Amptek software is shown in Figure 5. The spectrometer was positioned to capture photons scattered at an angle of 71.6° as this spectrum was acquired. Here, two peaks can be seen, the larger one in light blue on the left is the peak associated with Compton scattering. Because of the scattering angle, this peak is centered on an energy value of 55.1 keV. The smaller peak on the right is caused by the Thompson scattering of photons off of nuclei. These photons lose little energy, and as such, the peak is at 59.5 keV. The FWHM of the Compton peak, at 1.4 keV, is 2.5 times larger than that of the unscattered peak. The broadening of the Compton scattering peak and the surrounding backgrounds are primarily caused by scatterings from material around the sensor. A secondary effect is that slightly different angles of scattering are permitted by the collimator's size, which is expected to increase the FWHM by 0.2 keV. The ratio of the highlighted Compton scattering area to that of the highlighted Thompson scattering area is 6:1.

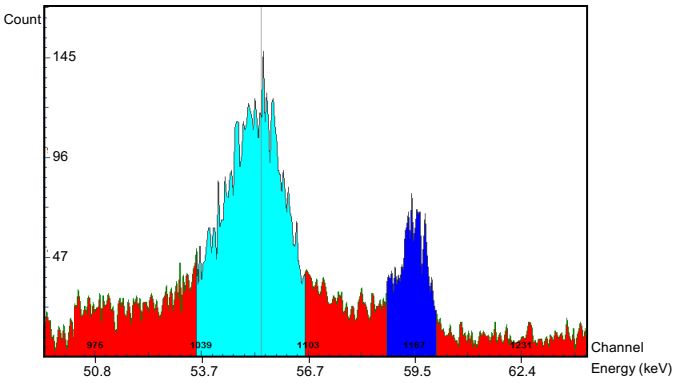

Figure 5: Example photon spectrum for Compton scattering of photons at an angle of 71.6°. The peak associated with Compton scattered photons is in light blue; the peak associated with Thompson scattered photons is in dark blue. The x-axis is in channel number, which is a value native to the spectrometer.

3 Example run and proof of principle

For the purposes of a calibration using Compton scattering, the RD53A was tuned to have a very low threshold and slow preamplifier return to baseline, as was discussed in Section 2. A histogram of each of pixel's threshold is shown in Figure 6 (a). The "goal" of this tuning was for each pixel to have a threshold of 450e, meaning that a charge injection of 450 electrons would create a readout with a ToT-code of 0. The average threshold achieved was 441e, which a standard deviation of 24e. Similarly, a histogram of all pixels' average ToT output due to a series of injections of 1000e is shown in Figure 6 (b). Because of the slow return to baseline, the mean ToT is 8.8 clock cycles. There is expected non-uniformity, or "dispersion", in the pixel response across the front-end, manifesting as a standard deviation of 1.8 clock cycles. As the charge-ToT relationship of each pixel is different, calibration must be performed on a per-pixel basis.

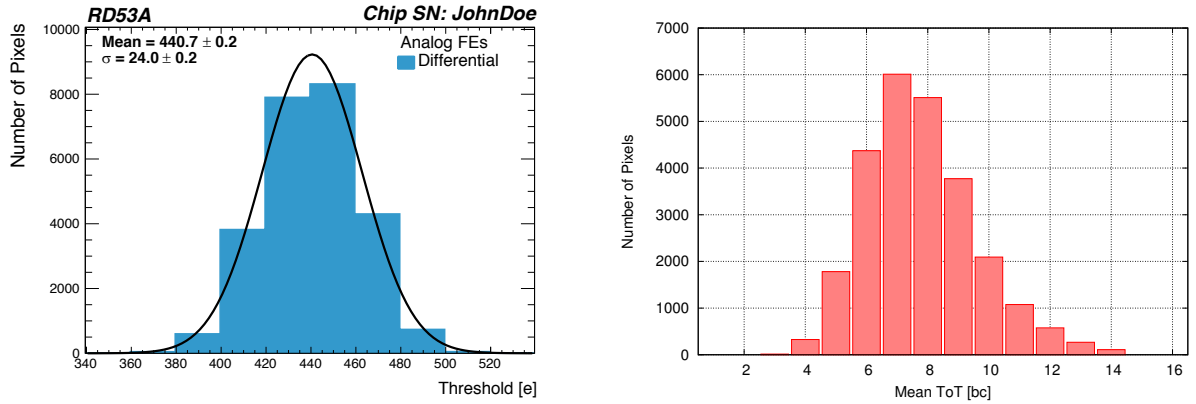

(a) (b)

Figure 6: (a) Histogram of the per-pixel threshold achieved in a chip tuning with a goal threshold of 450e. The average threshold achieved is 441e. (b) Histogram of all pixels' average ToT for repeated injections of 1000e. The average ToT across all pixels for such an injection is 8.76 clock cycles or bunch crossings (bc).

As a proof of principle of this calibration method, four scattering angles will be used:

- 51°, which corresponds to 2.5 keV of deposited energy or 690e of charge
- 56°, which corresponds to 3.0 keV of deposited energy or 830e of charge
- 63°, which corresponds to 3.7 keV of deposited energy or 1020e of charge.
- 67°, which corresponds to 4.1 keV of deposited energy or 1140e of charge.

As noted in Sections 2 and 2.1, the expected FWHM of the Compton scattering peak, accounting for extra broadening due to collimator aperture size, is 0.75 keV. Because of this, the distributions of ToT actually observed at each scattering angle will not be as clean as that seen in Figure 6 (b).

The spatial distribution of hits in the differential front end after 100 hours of running is shown in 7. These hits were read out based on a trigger caused by a photon being detected by the spectrometer, as described in Section 2.1. The hits shown have ToT in the range [2,13] in order to not show noise hits. The roughly circular distribution of hits is caused by the collimator, which was slightly off-center with respect to the differential front end.

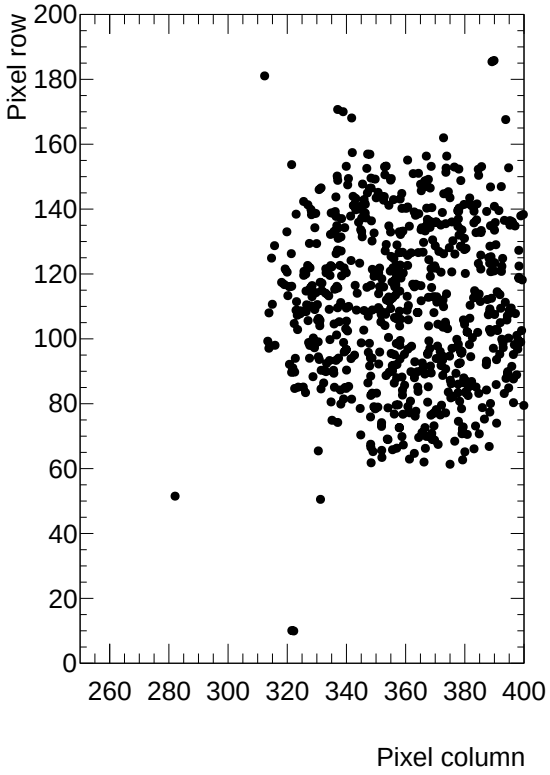

Figure 7: Spatial distribution of hits with ToT in the range [2,13] in the differential front end after a 100 hour run at 56°. The hits were associated with a Compton scattered photon detected by the spectrometer.

The ToT distributions of the hits associated with 100 hour runs at each of the four angles from above are shown in Figure 8. Similar to Figure 7 the ranges of the plots have been restricted so as to not show noise and overflow hits.

As mentioned above, the calibration is performed on a pixel-by-pixel basis. A series of charge injections are performed from 500e to 1500e in steps of 5e, which gives the ToT vs. injected charge function of each pixel. Two adjacent pixels' ToT response functions are shown in Figure 9, illustrating the diversity of such functions found in the front-end. Each pixel's plot is fit to a function of the form $a * \sqrt{x} + b + c * x + d * x^2$, such that each pixel has a unique set of $a,\ b,\ c,\ d$. In the Compton scattering runs, each hit is associated with an individual pixel. Plugging the charge associated with the photon's scattering angle into the above formula yields the "expected ToT" of each hit. This expected ToT can be compared to the actually observed ToT.

Figure 10 shows the distribution of per-pixel differences between the ToT of hits associated with Compton scattered photons and the expected ToT: (a), (b), (c), and (d) show the differences for 51°, 56°, 63°, 67° respectively. On average:

- The measured ToT for the 51° scattering is 1.1 clock cycles longer than expected.
- The measured ToT for the 56° scattering is 0.51 clock cycles longer than expected.
- The measured ToT for the 63° scattering is 0.40 clock cycles shorter than expected.
- The measured ToT for the 63° scattering is 1.4 clock cycles shorter than expected.

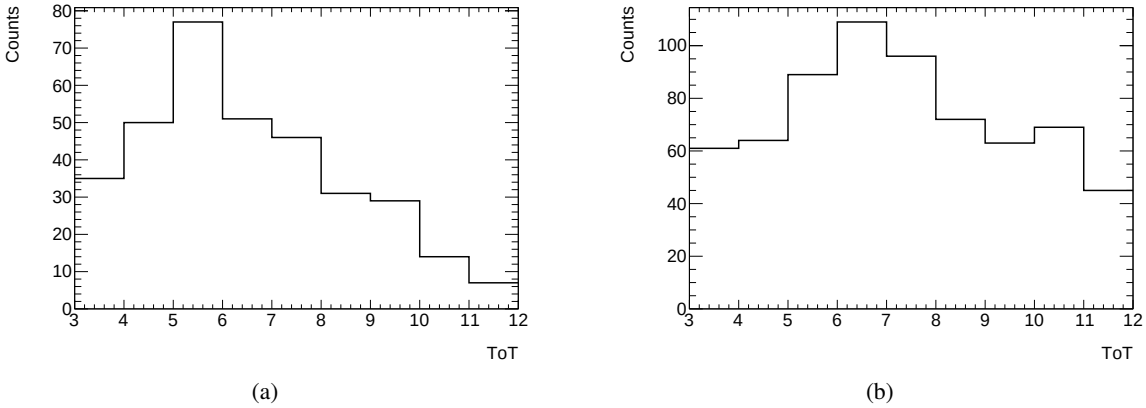

Figure 8: (a) Distribution of ToTs for hits associated with photons scattered at 51°. (b) Distribution of ToTs for hits associated with photons scattered at 56°. (c) Distribution of ToTs for hits associated with photons scattered at 53°. (c) Distribution of ToTs for hits associated with photons scattered at 67°.

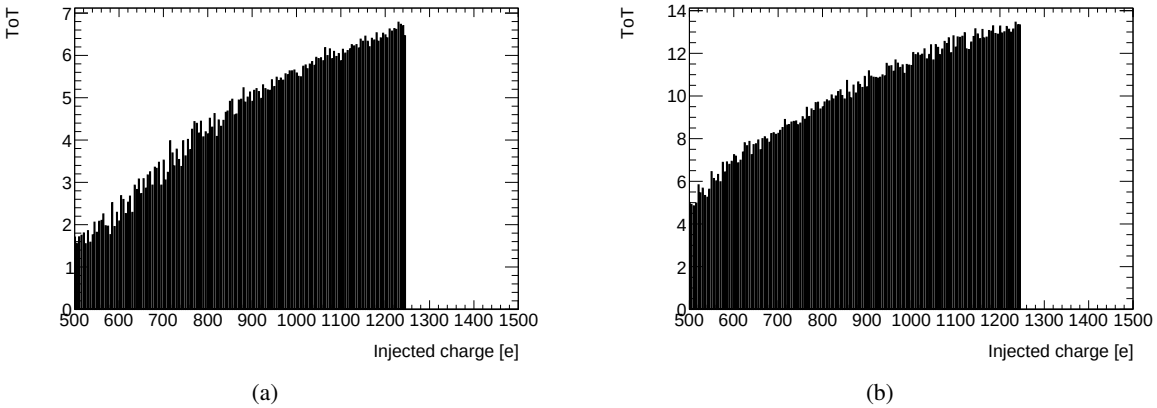

Figure 9: (a) Expected ToT as a function of injected charge for the pixel in row 189, column 351. (b) Expected ToT as a function of injected charge for the pixel in row 189, column 352. The shapes of the two functions are similar, but the ranges of ToT response are different.

Much of the dispersion in these plots is due to the width of the Compton scattering peak, as seen in Figure 5. The FWHM of photons associated with Compton scatters within the sensor is expected to be 0.75 keV, corresponding to a

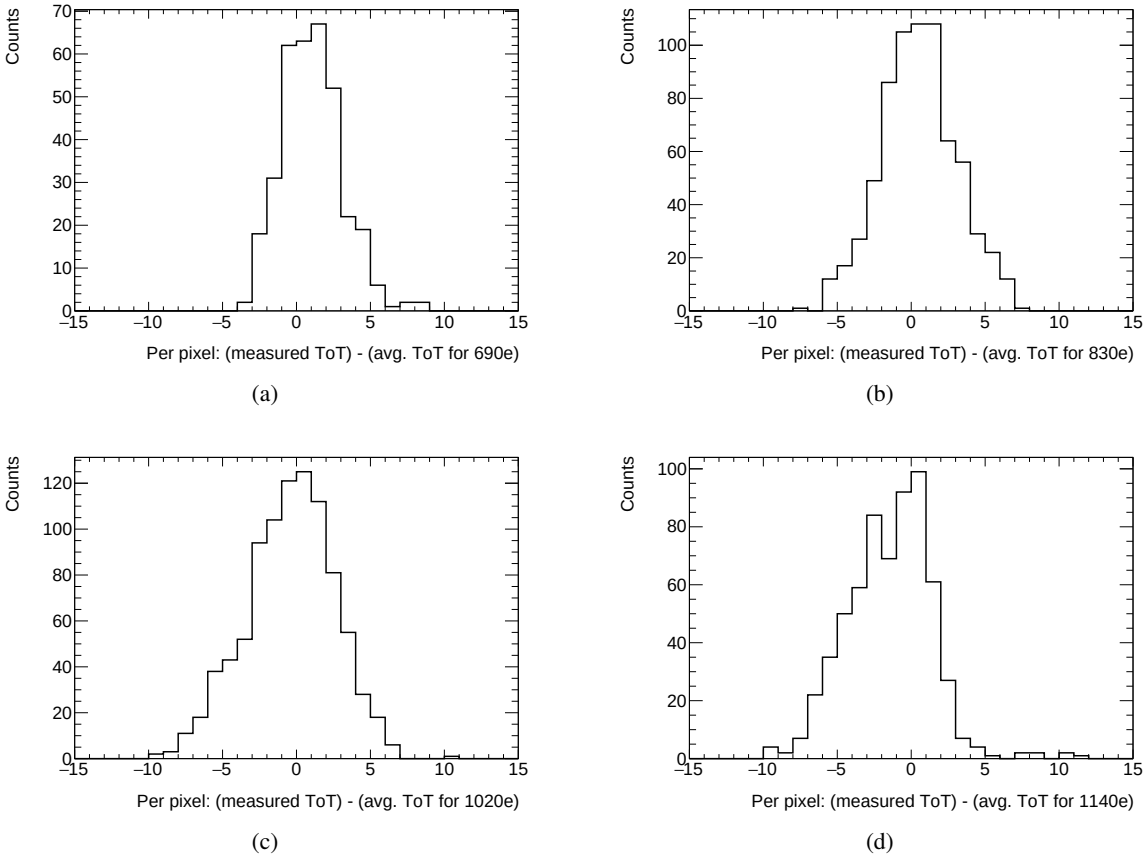

Figure 10: (a) Distribution of per-pixel differences between the ToT of hits from Compton scatters at 51° and the internal injection of the corresponding 690e. (b) Same for 56° and the internal injection of the corresponding 830e. (c) Same for 63° and the internal injection of the corresponding 1020e. (d) Same for 67° and the internal injection of the corresponding 1140e.

FWHM in charge units of 210e. Inspection of Figure 9 shows that such a range of charge injections corresponds to a difference in ToT response of about 2 clock cycles, depending on the particular pixel and the injected charge.

The mean values of these distributions are plotted against the expected charge deposit in Figure 11. A fit to line was performed, yielding a slope of -0.5 units of ToT per 100e difference in charge deposit for this particular tuning. A difference of 2.5 units of ToT is expected at the threshold injection of 440e.

4 Weaknesses of this method

The main weak point of this method is the time it takes to accumulate data. In these trials, about 6 events were observed per hour, leading to the necessity of long run times. This problem could be partially addressed by adjusting the setup: for example, by having the spectrometer cover a greater fraction of solid angle or using a larger collimator aperture. Another potential weak point is that the FWHM of the charge deposits distribution can be a significant fraction of the central value. In the trials shown here, it was up to 30%. This weakness can be addressed by the accumulation of significant amounts of data in order measure the central values with less uncertainty, unfortunately exacerbating the runtime problem.

5 Conclusion

We have presented here a new method for the calibration of thin silicon sensors with energies in the range of 1-10 keV using the Compton scattering of photons. The method was developed and tested using a 150 μm sensor bump-

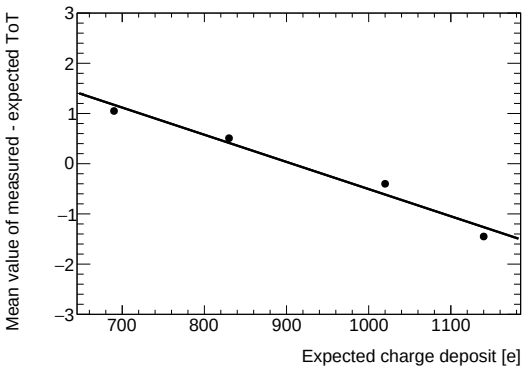

Figure 11: Plot of the mean values of the measured - expected ToT distributions found in Figure 10 as a function of the expected charge deposit. A linear trend line has been included with the four data points.

bonded onto an RD53A and an Americium-241 source. The physical setup involved a spectrometer that can be easily repositioned to enable calibrations at any desired energy within the achievable range. An example calibration was demonstrated, finding a trend in the difference between the ToT response to the external charge deposit and corresponding internal charge injection.

6 Acknowledgements

This work was supported by the U.S. Department of Energy, Office of Science under contract DE-AC02-05CH11231. Patrick McCormack was supported by the National Science Foundation Graduate Research Fellowship under Grant No. DGE 1752814. Any opinion, findings, and conclusions or recommendations expressed in this material are those of the author and do not necessarily reflect the views of the National Science Foundation.

References

[1] L. Evans and P. Bryan, "LHC Machine", JINST **3**, S08001 (2008).

[2] ATLAS Collaboration, "The ATLAS Experiment at the CERN Large Hadron Collider", JINST **3**, S08003 (2008).

[3] CMS Collaboration, "The CMS Experiment at the CERN LHC", JINST **3**, S08004 (2008).

[4] ATLAS Collaboration, "ATLAS pixel detector electronics and sensors", JINST **3**, P07007 (2008).

[5] ATLAS Collaboration, "ATLAS Insertable B-Layer Technical Design Report", ATLAS-TDR-19, https://cds.cern.ch/record/1291633 (2010).

[6] CMS Collaboration, "The Phase-1 Upgrade of the CMS Pixel Detector", JINST **17**, C07009 (2017).

[7] C. Hu-Guo et al., "CMOS pixel sensor development: A fast read-out architecture with integrated zero suppression", JINST **4**, P04012 (2009).

[8] M. Battaglia et al., "R&D Paths of Pixel Detectors for Vertex Tracking and Radiation Imaging", Nucl. Instrum. Meth. A **716** 29-45 (2013).

[9] M. Garcia-Sciveres and N. Wermes, "A review of advances in pixel detectors for experiments with high rate and radiation", Reports on Progress in Physics **81** 6 (2018).

[10] ATLAS Collaboration, "Operational Experience with the ATLAS Pixel Detector at LHC", PoS Vertex2012 (2013) 049, ATL-INDET-PROC-2012-031, https://cds.cern.ch/record/1498736.

[11] CMS Collaboration, "Calibration and performance of the CMS pixel detector in LHC Run 2", LHCP2019 (2019), arXiv:1909.12920 [physics.ins-det].

[12] CMS Collaboration, "Operational experience with the CMS pixel detector", JINST **10** 05 (2015).

[13] Zheng Li, "Radiation Hardness/Tolerance of Si Sensors/Detectors for Nuclear and High Energy Physics Experiments", Proceedings of the International Workshop on Semiconductor Pixel Detectors for Particles and X-Rays (PIXEL2002), https://www.slac.stanford.edu/econf/C020909/ (2002).

[14] A. H. Compton, "A Quantum Theory of the Scattering of X-Rays by Light Elements", Physical Review **21**, 5 (1923).

[15] O. Klein and Y. Nishina, "Über die Streuung von Strahlung durch freie Elektronen nach der neuen relativistischen Quantendynamik von Dirac", Z. Phys. **52**, 853-868 (1929).

[16] D. Pohl et al., "A method for precise charge reconstruction with pixel detectors using binary hit information", NIMA **788** (2015), 49-53.

[17] Ph. Bloch et al., "Silicon sensors for the CMS preshower detector", NIMA **479** (2002), 265-277.

[18] P. Zambon et al., "A wide energy range calibration algorithm for X-ray photon counting pixel detectors using high-Z sensor material", NIMA **925** (2019), 164-171.

[19] H. Ding et al., "Characterization of energy response for photon?counting detectors using x-ray fluorescence", Med. Phys. **41** 12 (2014).

[20] M. Das et al., "Energy calibration of photon counting detectors using x-ray tube potential as a reference for material decomposition applications", Proc. SPIE **9412** (2015).

[21] A. Bähr, P. Lechner, and J. Ninkovic, "Sensor development at the semiconductor laboratory of the Max-Planck-Society", JINST **12** (2017).

[22] RD53 Collaboration, "The RD53A Integrated Circuit", CERN-RD53-PUB-17-001 (2017), https://cds.cern.ch/record/2287593.

[23] M. Garcia-Sciveres et al., "The FE-I4 pixel readout integrated circuit", NIMA **636** (2011), 155-159.

[24] T. Poikela et al., "Timepix3: a 65K channel hybrid pixel readout chip with simultaneous ToA/ToT and sparse readout", JINST **9** (2014).

[25] T. Heim, "YARR - A PCIe based Readout Concept for Current and Future ATLAS Pixel Modules", J. Phys.: Conf. Ser. **898** 032053 (2017).

[26] R.H. Redus et al., "Design and performance of the X-123 compact X-ray and gamma-ray spectroscopy system," IEEE Nucl. Sci. Symp. Conf. Rec., 2006, R15-4.

[27] George Kour and Raid Saabne. Real-time segmentation of on-line handwritten arabic script. In *Frontiers in Handwriting Recognition (ICFHR), 2014 14th International Conference on*, pages 417–422. IEEE, 2014.

[28] George Kour and Raid Saabne. Fast classification of handwritten on-line arabic characters. In *Soft Computing and Pattern Recognition (SoCPaR), 2014 6th International Conference of*, pages 312–318. IEEE, 2014.

[29] Guy Hadash, Einat Kermany, Boaz Carmeli, Ofer Lavi, George Kour, and Alon Jacovi. Estimate and replace: A novel approach to integrating deep neural networks with existing applications. *arXiv preprint arXiv:1804.09028*, 2018.